Taylor & Francis
Taylor & Francis Group

Journal of Enzyme Inhibition and Medicinal Chemistry

ISSN: (Print) (Online) Journal homepage: https://www.tandfonline.com/loi/ienz20

Benzenesulfonamide derivatives as *Vibrio cholerae* carbonic anhydrases inhibitors: a computational-aided insight in the structural rigidity-activity relationships

Marialuigia Fantacuzzi, Ilaria D'Agostino, Simone Carradori, Francesco Liguori, Fabrizio Carta, Mariangela Agamennone, Andrea Angeli, Filomena Sannio, Jean-Denis Docquier, Clemente Capasso & Claudiu T. Supuran

To cite this article: Marialuigia Fantacuzzi, Ilaria D'Agostino, Simone Carradori, Francesco Liguori, Fabrizio Carta, Mariangela Agamennone, Andrea Angeli, Filomena Sannio, Jean-Denis Docquier, Clemente Capasso & Claudiu T. Supuran (2023) Benzenesulfonamide derivatives as *Vibrio cholerae* carbonic anhydrases inhibitors: a computational-aided insight in the structural rigidity-activity relationships, Journal of Enzyme Inhibition and Medicinal Chemistry, 38:1, 2201402, DOI: 10.1080/14756366.2023.2201402

To link to this article: https://doi.org/10.1080/14756366.2023.2201402

JOURNAL OF ENZYME INHIBITION AND MEDICINAL CHEMISTRY
2023, VOL. 38, NO. 1, 2201402
https://doi.org/10.1080/14756366.2023.2201402

Taylor & Francis
Taylor & Francis Group

RESEARCH PAPER

OPEN ACCESS Check for updates

Benzenesulfonamide derivatives as *Vibrio cholerae* carbonic anhydrases inhibitors: a computational-aided insight in the structural rigidity-activity relationships

Marialuigia Fantacuzzi[a]*, Ilaria D'Agostino[a]*, Simone Carradori[a], Francesco Liguori[a], Fabrizio Carta[b], Mariangela Agamennone[a], Andrea Angeli[b], Filomena Sannio[c], Jean-Denis Docquier[c,d], Clemente Capasso[e] and Claudiu T. Supuran[b]

[a]Department of Pharmacy, "G. d'Annunzio" University of Chieti-Pescara, Chieti, Italy; [b]Neurofarba Department, Section of Pharmaceutical and Nutraceutical Sciences, University of Florence, Florence, Italy; [c]Department of Medical Biotechnologies, University of Siena, Siena, Italy; [d]InBioS, Centre for Protein Engineering, University of Liège, Liège, Belgium; [e]Department of Biology, Agriculture and Food Sciences, National Research Council (CNR), Institute of Biosciences and Bioresources, Naples, Italy

ABSTRACT

Vibrio cholerae causes life-threatening infections in low-income countries due to the rise of antibacterial resistance. Innovative pharmacological targets have been investigated and carbonic anhydrases (CAs, EC: 4.2.1.1) encoded by *V. cholerae* (*Vch*CAs) emerged as a valuable option. Recently, we developed a large library of *para*- and *meta*-benzenesulfonamides characterised by moieties with a different flexibility degree as CAs inhibitors. Stopped flow-based enzymatic assays showed strong inhibition of *Vch*αCA for this library, while lower affinity was detected against the other isoforms. In particular, cyclic urea **9c** emerged for a nanomolar inhibition of *Vch*αCA (K_I = 4.7 nM) and high selectivity with respect to human isoenzymes (SI≥ 90). Computational studies revealed the influence of moiety flexibility on inhibitory activity and isoform selectivity and allowed accurate SARs. However, although *Vch*CAs are involved in the bacterium virulence and not in its survival, we evaluated the antibacterial activity of such compounds, resulting in no direct activity.

GRAPHICAL ABSTRACT

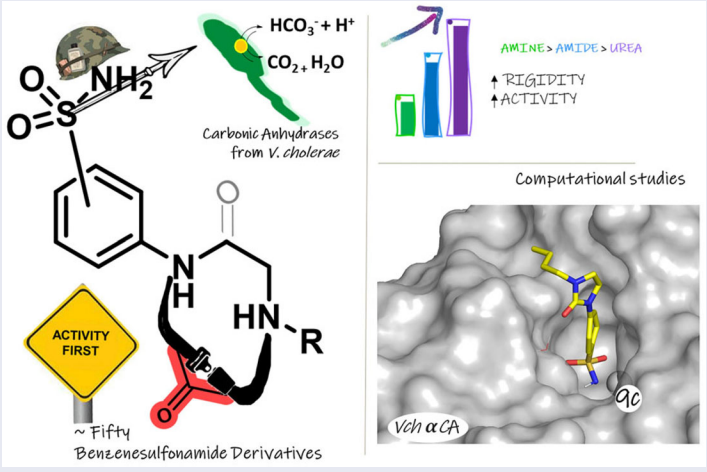

ARTICLE HISTORY
Received 22 February 2023
Revised 30 March 2023
Accepted 4 April 2023

KEYWORDS
Carbonic anhydrase; sulfonamides; *Vibrio cholerae*; imidazolidinone; isoform selectivity; homology modelling; docking; MD

Introduction

The COVID-19 pandemic represented an unanticipated global issue, responsible for over 6.8 M deaths worldwide and a big concern in Public Healthcare in relation to the impairment of human immune defences, thus unable to fight secondary microbial infections that became potentially fatal[1]. However, besides these direct and economic burdens, the outbreak of COVID-19 was also responsible for the crowding of hospitals and the consequent slowing down of other disease treatments and surgery, such as those related to cancer patients[2]. Moreover, underdeveloped countries significantly suffered from the COVID-19 disruption of humanitarian aid programs, fundamental in the life-saving safe water, sanitation, and hygiene (WASH) techniques and the diagnosis, treatment, and vaccination

CONTACT Simone Carradori simone.carradori@unich.it Department of Pharmacy, "G. d'Annunzio" University of Chieti-Pescara, 66100 Chieti, Italy
*These authors contribute equally.

Supplemental data for this article can be accessed online at https://doi.org/10.1080/14756366.2023.2201402.

campaigns for those diseases, such as cholera, that are a passed threat for industrialised countries[3,4].

Cholera, also referred to as "blue death", is an acute diarrheal illness that became fatal if left untreated (50–70% mortality rate) and provoked seven pandemics till the 19th century and a consequent number amounting to an impressive 143 000 deaths per year[5]. In recent years, its incidence is most evident in those areas with low hygienic conditions and limited access to safe drinking water and food, in particular after cataclysmic events or during armed conflicts, such as sub-Saharan African countries, *i.e.* Niger, Nigeria, Ethiopia, and Sudan, India, and Bangladesh[6–8]. The alarming data from these areas envisaged the institutions of a worldwide strategy to control the disease named "Ending Cholera: a global roadmap to 2030" in 2017 aimed at reducing mortality by 90%. However, a significative increase in reported cholera cases was noticed during the COVID-19 pandemic compared to previous years[7].

Cholera aetiology is related to the infection by the Gram-negative curved rod-shaped *Vibrio cholerae,* but only two serogroups, O1 and O139, can cause illness[9], characterised by a massive loss of water and electrolytes, resulting in severe dehydration and hypovolemic shock. Thus, the pharmacological therapies are usually based on intravenous rehydration and the administration of antibiotics, such as a single dose of doxycycline as first-line treatment, erythromycin, azithromycin, norfloxacin, ciprofloxacin, and trimethoprim-sulfamethoxazole combination[10]. However, several cases of bacterial resistance were reported[11–14] and make the search for new antibiotics and their development urgently needed, although some oral vaccines (the FDA-licensed Vaxchora® and the WHO-prequalified Dukoral®, ShanChol®, and Euvichol-Plus®/Euvichol®) are already in clinical use.

In the last decades, carbonic anhydrases (CAs, E.C. 4.2.1.1) emerged for their multifaceted physio-pathological roles and, thus, their high potential as pharmacological targets in medicinal chemistry and the antibacterial field[15]. CAs are ubiquitous metalloenzymes involved in the physiological balance between carbonic dioxide and bicarbonate anion in the cell, thus governing the pH homeostasis, the secretion of electrolytes, the carboxylation reactions, and other metabolic pathways[16,17]. Herein, the interest in inhibiting CAs with antibacterial purposes is amply justified and recently confirmed in *in vivo* studies[18–22].

The genome of *V. cholerae* species encodes for three CAs, belonging to three of the eight different classes of CA isoforms: the α-, also present in mammalians, and the β- and the γ-isoenzymes[23,24]. Although the role of *Vch*CAs has not been well established yet, accumulating evidence relates their function to the etiopathogenesis of the *V. cholerae* infection[25]. After the invasion of the host and the colonisation of the upper small intestine epithelial layer, the pathogen penetrates the mucus and attaches to the microvilli via the bacterial pili, where it releases its endotoxin (cholera toxin, CT), the main virulence factor, that triggers the increased secretion of water, sodium and potassium cations and bicarbonate anion into the lumen of the intestine, leading to severe dehydration[26]. The small intestine maintains an alkaline pH environment through the pancreatic release of sodium bicarbonate, an inducer of the CT expression[25]. However, the absence of genes encoding for bicarbonate transporters in *V. cholerae* lets us hypothesise the use of CAs as a bicarbonate-assimilating system in the cell.

Moreover, as assessed through the STRING web tool (https://string-db.org/ accessed on March 4th, 2022)[27], *Vch*CAs participate in several functional and physical protein-protein association networks, such as proteins belonging to the sulfate permease family, those involved in the degradation of long-chain fatty acids, fumarate hydratase, uridine kinase, etc. Relevantly, *Vch*CAs also seem to be associated with the thioredoxin system, fundamental in the physiology and pathogenesis of bacteria due to its influence on the expression of many genes, in the reduction of cytoplasmic proteins and hydrogen peroxide and, in general, cell division, energy transduction, oxidative stress response, transcriptional regulation, phage assembly and propagation[28].

After the isolation and characterisation of the three isoenzymes from *V. cholerae*[29,30], several studies have been reported on the development of potent inhibitors, most of them selective, endowed with different chemical scaffolds[31], such as benzoxaboroles[32], indole-based hydrazones[33], sulfamides (-$NHSO_2NH_2$)[34], *N*-hydroxy-ureas[35], and differently substituted benzenesulfonamides designed through the tail approach[36–39].

We recently developed a series of benzenesulfonamides as antitumor agents, highlighting, in some cases, a clear trend in the inhibitory profile according to the presence of specific moieties able to confer different rigidity to the chemical structure (Figure 1)[40,41].

However, the compounds showed no higher selectivity towards the enzymes of interest, CA IX and CA XII, with respect to the cytosolic isoforms I and II. Thus, we investigated the possible inhibition of one or more different CAs, such as those from the bacterial *V. cholerae*.

Results and discussion

Rationale and preparation of the library

The derivatives design was inspired by *the tail approach*, a MedChem strategy that has been applied for the first time in the CA inhibition field in 1999[42,43]. In the beginning, it was aimed to enhance the pharmacokinetic properties of such compounds[44], then, it was largely employed to address the isoform selectivity issue. Generally, tailed CA inhibitors are composed of three elements: a zinc-binding group (ZBG, in red, Figure 2), a main scaffold with a spacer (in cyan, Figure 2), and the hydrophobic tail (in light green, Figure 2).

This strategy is based on the idea to allow the compound zinc-binding group to reach the enzyme metal in the binding cavity and to establish a complex and well-defined interaction network with the isoform-specific enzyme residues (most of which are

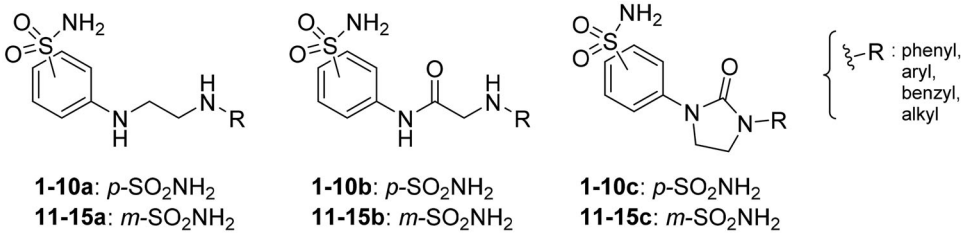

1-10a: *p*-SO_2NH_2 **1-10b**: *p*-SO_2NH_2 **1-10c**: *p*-SO_2NH_2
11-15a: *m*-SO_2NH_2 **11-15b**: *m*-SO_2NH_2 **11-15c**: *m*-SO_2NH_2

Figure 1. Compounds investigated in this work.

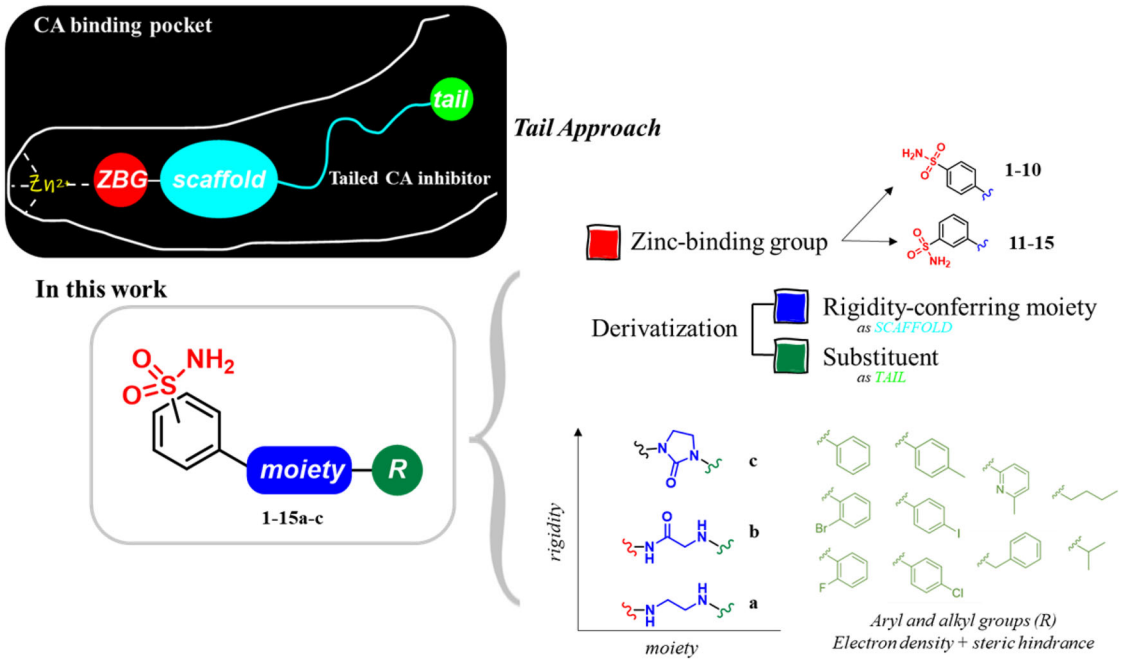

Figure 2. Overview of the tail approach and the design strategy used in the current work.

hydrophobic) in the entry of the binding site through the scaffold and tail portions.

In the current work, the design of derivatives **1–15a–c** involved the use of 4- and 3-benzenesulfonamides as zinc-binding groups (in red, Figure 2) and different derivatization elements as binary systems composed of flexibility/rigidity-conferring moiety (in blue, Figure 2), such as the amine (**a**), the amide (**b**), and the cyclic urea (**c**) function (in increasing order of rigidity in Figure 2), in lieu of the traditional scaffold-spacer component, and a specific aryl or alkyl substituent (R, in green, Figure 2) endowed with different electron density and steric hindrance properties as the compound tail.

Aimed at exploring the enzymatic inhibitory profile of the library of compounds **1–15a–c** and discovering promising activities for further development as antibacterial agents, we evaluated their ability to inhibit the three CAs from the pathogen *V. cholerae*. Compounds **1–15a–c** were prepared as reported[40].

In vitro inhibition of VchCAs and preliminary SAR considerations

The inhibition profiles for sulfonamides **1–15a–c** and the reference **AAZ** against α-, β-, and γ-CAs from *V. cholerae* were determined through the stopped-flow CO_2 hydrase assay[45], and as a comparison, inhibitory data on the physiologically relevant *h*CAs I and II are reported as inhibition constants (K_Is) (Table 1).

Based on the reported inhibition data, several structure-activity-relationship (SAR) considerations can be drawn, especially regarding inhibition spectrum and selectivity. Overall, all the compounds showed a nanomolar inhibitory activity against *h*CAs I and II[40].

Furthermore, the assessment of the inhibitory activity on α-CA from *V. cholerae* highlights the structural differences among the binding pockets of the human and bacterial enzymes. The *in vitro* experiments seem to confirm the bigger size of the *Vch*αCA binding pocket, as outlined by the good activity of the 4-iodophenyl (**4a**) and 2-bromophenyl (**5a**) derivatives. Remarkably, pyridinyl-bearing compound **7b** results to be the most active among the amido library (scaffold **b**), while the bulky alkyl substituent of **10a** confers a higher potency to the amino *para*-series (scaffold **a**). The rigidity of scaffold **c** contributes to reducing the K_I values, resulting in notable inhibitory profiles for almost all the *para*-sulfonamides and monosubstituted phenyl derivatives **12–14c**. In general, all tested cyclic compounds were found active in inhibiting the target enzymes, even if they failed to reach the high potency of **AAZ** in some cases, especially for those endowed with scaffolds **a** and **b**.

The whole set of compounds exerts a less potent inhibitory activity on the β-CA isoform of *V. cholerae*, as shown by the K_Is in the micromolar range. Low activity was found for halophenyl derivatives characterised by **a** scaffold (**4–6a** and **14a**). Also, the same trend of inhibition was observed for the acyclic derivatives, highlighting a better activity profile of the bulky **10a** than the linear derivatives **9a** and **15a**. Regarding the aromatic moieties on scaffold **b**, the unsubstituted phenyl ring positively affects the activity, conferring the best inhibitory profile among the para-series (**1b**) and the worst among the *meta*-series (**11b**). However, the most active amide is the *i*-propyl compound **10b** with a K_I value of 4.0 μM.

Finally, the tested compounds show a very low (in the micromolar range) activity on the γ isoform. In particular, in the *para*-benzenesulfonamide amine series (scaffold **a**) the inactivity of the phenyl derivative **1a** seems to be restored only in the presence of an electron donor (methyl) substituent on the ring (**2a**), while the introduction of one halogen in *para* or *ortho* position (**3–5a**) still corresponds to a lack of activity, except for the fluorophenyl compound **6a**. Not relevant K_I values were also detected on the other derivatives. Inactivity also for the phenyl derivative in the *meta*-**a** series (**11a**), but this time, restored by tolyl moiety in **12a** and still improved by the chlorophenyl derivative **13a**. The butyl tail improves the *Vch*γCA inhibition in the *meta*-series (**15a**) with respect to the *para*- one (**9a**). In the **b** library, the only interesting

Table 1. Inhibition data of sulfonamides **1–15a–c** and reference compound **AAZ** on *h*CAs I and II and *Vch*CAs through the stopped-flow CO_2 hydrase assay.

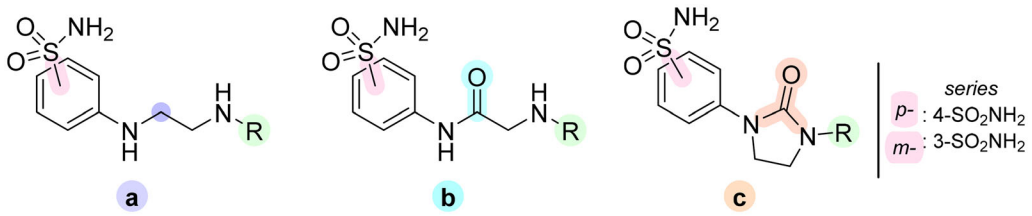

				K_I (nM)						
Cpd	Scaffold	Series	*R*	*h*CA Ia	*h*CA II[a]	*Vch*αCA	*Vch*βCA	*Vch*γCA	SI [$\frac{KI\ hCA\ I}{KI\ VchαCA}$]	SI [$\frac{KI\ hCA\ II}{KI\ VchαCA}$]
1	**a**	*p-*		25.4	7.2	78.1	18 300	n.a.	0.3	0.1
2	**a**	*p-*	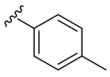	9.7	3.1	43.1	16 800	39 900	0.2	0.1
3	**a**	*p-*	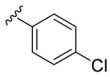	39.0	47.0	27.4	53 800	n.a.	1.4	1.7
4	**a**	*p-*	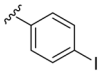	787	646	65.0	136 400	n.a.	12.1	9.9
5	**a**	*p-*		939	908	64.1	89 200	n.a.	14.7	14.2
6	**a**	*p-*		75.3	8.2	36.2	100 800	73 700	2.1	0.2
7	**a**	*p-*		87.0	31.4	37.0	19 000	69 800	2.4	0.9
8	**a**	*p-*	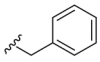	169	32.7	23.0	12 400	52 700	7.4	1.4
9	**a**	*p-*	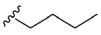	538	82.2	78.8	115 000	n.a.	6.8	1.0
10	**a**	*p-*		896	338	7.5	12 500	92 900	119.5	45.0
11	**a**	*m-*		7.0	4.1	63.0	15 600	n.a.	0.1	0.1
12	**a**	*m-*	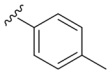	>1000	901	44.1	173 200	79 000	>22.7	20.4
13	**a**	*m-*	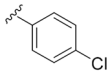	346	15.7	75.6	59 200	5600	4.6	0.2
14	**a**	*m-*		7.6	3.3	63.5	97 000	n.a.	0.1	0.1
15	**a**	*m-*	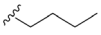	151	43.2	80.3	56 500	69 300	1.9	0.5
1	**b**	*p-*		62.6	3.2	53.0	17 700	49 400	1.2	0.1

(*continued*)

Table 1. Continued.

Cpd	Scaffold	Series	*R*	K_I (nM) *h*CA Ia	*h*CA II[a]	*Vch*αCA	*Vch*βCA	*Vch*γCA	SI [$\frac{KI\ hCA\ I}{KI\ Vch\alpha CA}$]	SI [$\frac{KI\ hCA\ II}{KI\ Vch\alpha CA}$]
2	**b**	*p*-	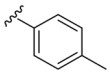	6.6	82.4	43.1	97 000	82 600	0.2	1.9
3	**b**	*p*-	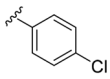	16.7	6.0	66.0	116 400	86 900	0.3	0.1
4	**b**	*p*-	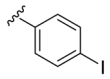	>1000	909	22.8	157 300	72 500	>43.9	39.9
5	**b**	*p*-		29.8	3.0	62.0	47 400	87 700	0.5	0.1
6	**b**	*p*-		18.4	4.8	79.0	51 400	93 100	0.2	0.1
7	**b**	*p*-		15.3	4.7	17.0	73 100	59 800	0.9	0.3
8	**b**	*p*-	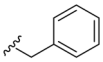	26.5	5.0	61.4	53 200	n.a.	0.4	0.1
9	**b**	*p*-	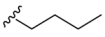	160	8.4	78.6	141 400	n.a.	2.0	0.1
10	**b**	*p*-		92.0	26.6	36.2	4000	58 300	2.5	0.7
11	**b**	*m*-		443	35.5	59.4	132 500	n.a.	7.5	0.6
12	**b**	*m*-	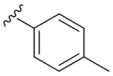	86.4	8.2	73.1	120 800	9600	1.2	0.1
13	**b**	*m*-	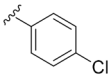	269	32.4	75.5	70 400	n.a.	3.6	0.4
14	**b**	*m*-		20.3	86.0	72.3	16 000	72 400	0.3	1.9
15	**b**	*m*-	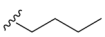	83.7	37.4	66.4	116 400	73 600	1.3	0.6
1	**c**	*p*-		54.4	4.3	7.1	134 000	5000	7.7	0.6
2	**c**	*p*-	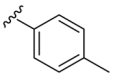	16.1	3.7	27.0	83 600	3500	0.60	0.14
3	**c**	*p*-	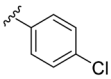	194	46.3	47.0	106 000	50 200	4.1	1.0
4	**c**	*p*-	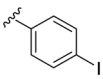	92.7	13.0	13.0	116 000	72 200	7.1	1.0

(*continued*)

Table 1. Continued.

Cpd	Scaffold	Series	R	K_I (nM)					SI $[\frac{KI\ hCA\ I}{KI\ Vch\alpha CA}]$	SI $[\frac{KI\ hCA\ II}{KI\ Vch\alpha CA}]$
				*h*CA Ia	*h*CA II[a]	*Vch*αCA	*Vch*βCA	*Vch*γCA		
5	**c**	*p*-		6.2	3.4	47.2	n.a.	73 200	0.1	0.1
6	**c**	*p*-		7.8	3.1	9.7	108 000	82 800	0.8	0.3
7	**c**	*p*-		54.6	7.2	11.0	122 000	80 200	5.0	0.7
8	**c**	*p*-	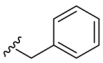	8.0	3.1	2.6	127 200	8100	3.1	1.2
9	**c**	*p*-	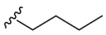	604	423	4.7	113 100	54 900	128.4	90.0
10	**c**	*p*-		8.5	3.2	9.8	113 200	64 500	0.9	0.3
11	**c**	*m*-		60.6	31.1	50.3	100 200	6500	1.2	0.6
12	**c**	*m*-	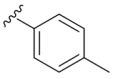	462	500	11.0	n.a.	76 000	42.0	45.5
13	**c**	*m*-	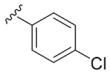	30.3	84.1	4.0	121 800	73 700	7.6	21.0
14	**c**	*m*-		8.0	54.4	10.0	132 100	81 300	0.8	5.4
15	**c**	*m*-	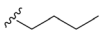	36.3	8.0	47.0	122 000	8000	0.8	0.2
AAZ				250	12.1	6.8	451	473	36.8	1.8

K_I values are reported as means of three independent experiments by a stopped-flow technique. Errors are in the range of ± 5–10% of the reported values. Acetazolamide (AAZ) was used as a reference control in these assays. *Vch*CAs are from *V. cholerae* species. Selectivity index (SI) values are calculated as indicated in the table. Compounds are presented based on the molecular scaffold (***a***, amine, ***b***, amide, and ***c***, urea) and the (*meta*- or *para*-) position with respect to the benzenesulfonamide core. n.a.: not active at 100 μM.
[a]Data from Ref. 40.

compound, with a K_I of 9.6 μM, bears the tolyl ring (**12b**) in the *meta*-series. The cyclic ureas (scaffold **c**) show notably low micromolar activities, especially for the unsubstituted phenyl derivatives (**1c** and **11c**).

The panel of tested CAs in Table 1 seems to suggest a promising development of this library of derivatives against *V. cholerae* enzymes. In fact, although the moderate-low activity against *Vch*βCA and *Vch*γCA, a relevant inhibitory profile emerged for several compounds and, in some cases, a good selectivity on the bacterial α isoform with respect to the human ones is gained. Indeed, selectivity index (SI) values on *h*CA I reported in Table 1 show that the presence of a 4-chlorophenyl ring and the *n*-butyl tail are helpful to address the activity on *Vch*αCA for all the investigated scaffolds, while the tolyl group helps to gain selectivity only in the *meta*-series also towards the human isoform II. Considering the aromatic groups, the *h*CA I/*Vch*αCA selectivity is also reached by derivatives endowed with a phenyl ring on scaffolds **b** and **c** and the pyridinyl and benzyl functions in the *para*-series of scaffolds **a** and **c**. However, several compounds display a good *h*CA II/*Vch*αCA selectivity, even if with a different trend. Overall, the amino compound **10a**, the amido **4b**, and the ureidic **9c** and **12c** emerged as the most selective derivatives, with higher human/-bacterial SI than **AAZ**.

We could argue that the increase in rigidity from the most flexible amino tail (scaffold **a**) to the amido (**b**) and cyclic urea (**c**) functions corresponds to an enhancement of the inhibitory activity of this class of compounds, maybe due to a different binding mode. However, clear evidence of the optimal sulfonamide moiety (*meta* or *para*) position on the structural nucleus could not be found from the *in vitro* assay results. In general, it is not trivial to draw accurate SARs with a large amount of experimental data, and a computational structure-based study of compounds into the binding pockets of the targeted enzymes could help the understanding of their inhibition and affinity.

In silico studies

Flexibility properties calculation

The structural flexibility of studied ligands was assessed through the FAFDrugs4 webserver (FAFDrugs4, https://fafdrugs4.rpbs.

Table 2. Flexibility properties of compounds **1a–c** and **9a–c**, selected as representative of the whole library of derivatives, calculated through FAFDrugs4 webtool.

CPD	Structure	Flexibility	Rotable bonds (#)	Rigid bonds (#)
1a	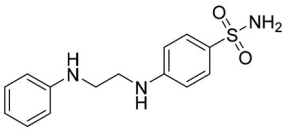	0.30	6	14
1b	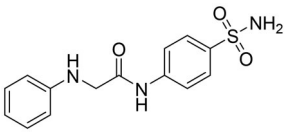	0.24	5	16
1c	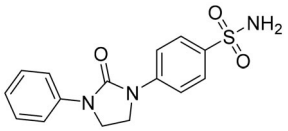	0.13	3	20
9a	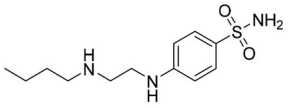	0.50	8	8
9b	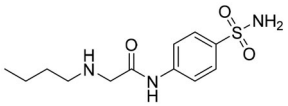	0.41	7	10
9c	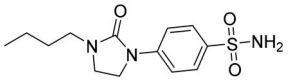	0.26	5	14

univ-paris-diderot.fr/)[46], considering the number of rigid and flexible bonds as established by Veber rules[47]. Examples of the calculated values are reported in Table 2.

Observing data in Table 2, the same trend was noticed for both the phenyl substituted derivative **1** and the alkyl compound **9**, reported as representatives of the whole library of compounds. The flexibility value decreases within the series **a**–**b**–**c** from the amine (**a**) to the urea (**c**) in correspondence to the increase in the number of the rigid bond. However, very different values were obtained for **1** and **9**, since the aliphatic tail belonging to the latter is very flexible with respect to the aromatic ring of **1**. In fact, as expected, the alkyl derivatives **9a–c** hold a flexibility value higher than both **1b** and **1c**. In this study, we tried to better understand how this broad range of flexibility of the tails, also considering the different interactions they can establish with the enzyme residues, could affect the affinity and, thereby, the inhibitory activity of the compound.

Molecular docking and MD simulations on the VchαCA

To shed light on the binding mode of our benzenesulfonamide inhibitors, structure-based studies of all compounds in *Vch*CAs and *h*CAs were conducted.

Since the 3D coordinates of *Vch*αCA are not included in the PDB database, a homology modelling protocol has been applied. The *Vch*αCA model was based on the experimental coordinates of *Photobacterium profundus* (PDB: 5HPJ), showing the highest sequence identity (64.75%). During our study, the 3D structure of this protein predicted by AlphaFold2[48] was made available in the AlphaFold Protein Structure Database (https://alphafold.ebi.ac.uk/) and was compared with the structure generated by homology modelling. The RMSD value for *Vch*αCA was 0.838 Å underpinning the validity of our model. To optimise residue positioning around the sulfonamide group, the AAZ geometry derived from the crystallographic complex with the αCA from *Helicobacter pylori* (PDB: 4YGF) was placed in the binding site after the proper alignment of the three zinc-coordinating histidine residues (His104, His106, and His123). To relax the protein with the known sulfonamide, the complex of the HM-*Vch*αCA and AAZ was minimised, and the obtained protein was used for the docking studies.

The docked poses reveal that all compounds assume a similar placement in the active site. The sulfonamide NH group, negatively charged, coordinates the zinc ion by a tetrahedral geometry and establishes an H-bond with the hydroxyl group of Thr189, while one of the sulphonyl oxygen H-bonds to the NH of the Thr189 backbone. We noticed a different binding mode depending on the position of the substituent: most *para*-substituted compounds point towards the *Vch*αCA coil (residues 128–132) (Figure 3(A,B,E–H)), while *meta*-substituted compounds move in the opposite direction (Figure 3(C,D)).

Considering the linker between the benzenesulfonamide portion and the R-group, more constrained compounds bearing the cyclic urea (**1**–**15c**) show a further H-bond between the cyclic carbonyl and, alternatively, Gln102 for *para*-substituted (**9c**, Figure 3(A,B)), or Thr190 backbone NH for *meta*-substituted (**12c**, Figure 3(C,D)). Compounds containing the amide linker show the same H-bond with Gln102 for *para*-sulfonamides, while the H-bond with Thr190 was conserved only for **4b** for *meta*-substituted (Figure 3(E,F)).

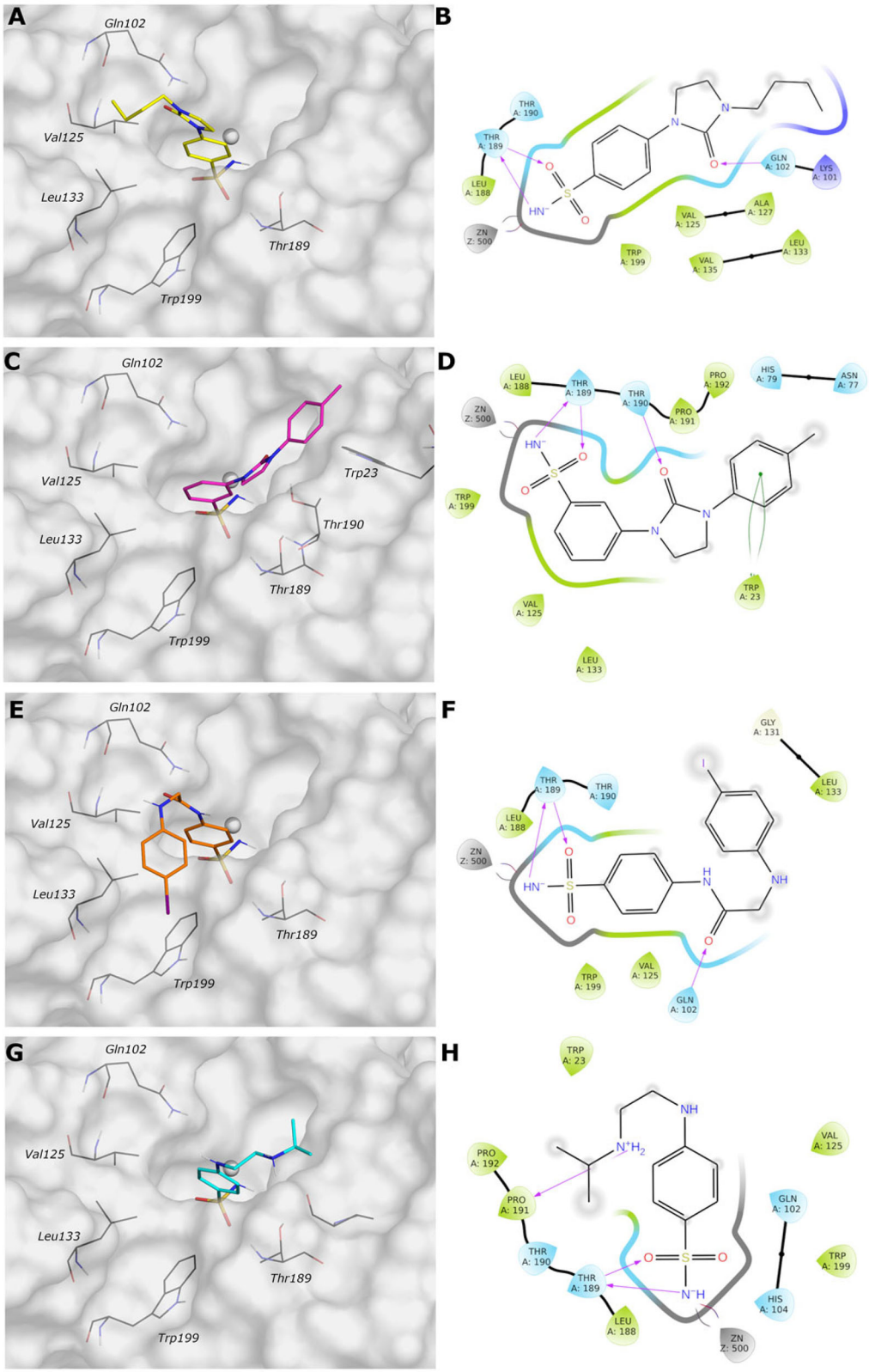

Figure 3. (A, C, E, and G) Predicted 3D binding mode and (B, D, F, and H) corresponding ligand interaction diagram of most selective ligands (A, B) **9c** yellow, (C, D) **12c** magenta, (E, F) **4b** orange, and (G, H) **10a** cyan, within *Vch*αCA (light grey). The compounds are represented as sticks, and the protein surface is visualised.

In the *para*-substituted series with the more flexible linker, the amine group, only compound **10a** (Figure 3(G,H)) makes an additional H-bond between the distal amine and the Pro190 carbonyl, preferring a different placement on the active site with respect to the other *para*-compounds. To obtain more insight into the binding process, 100 ns MD simulations on the *Vch*αCA complexes with most selective inhibitors **9c**, **12c**, **4b**, and **10a** were carried out (Figure 4(A–D)).

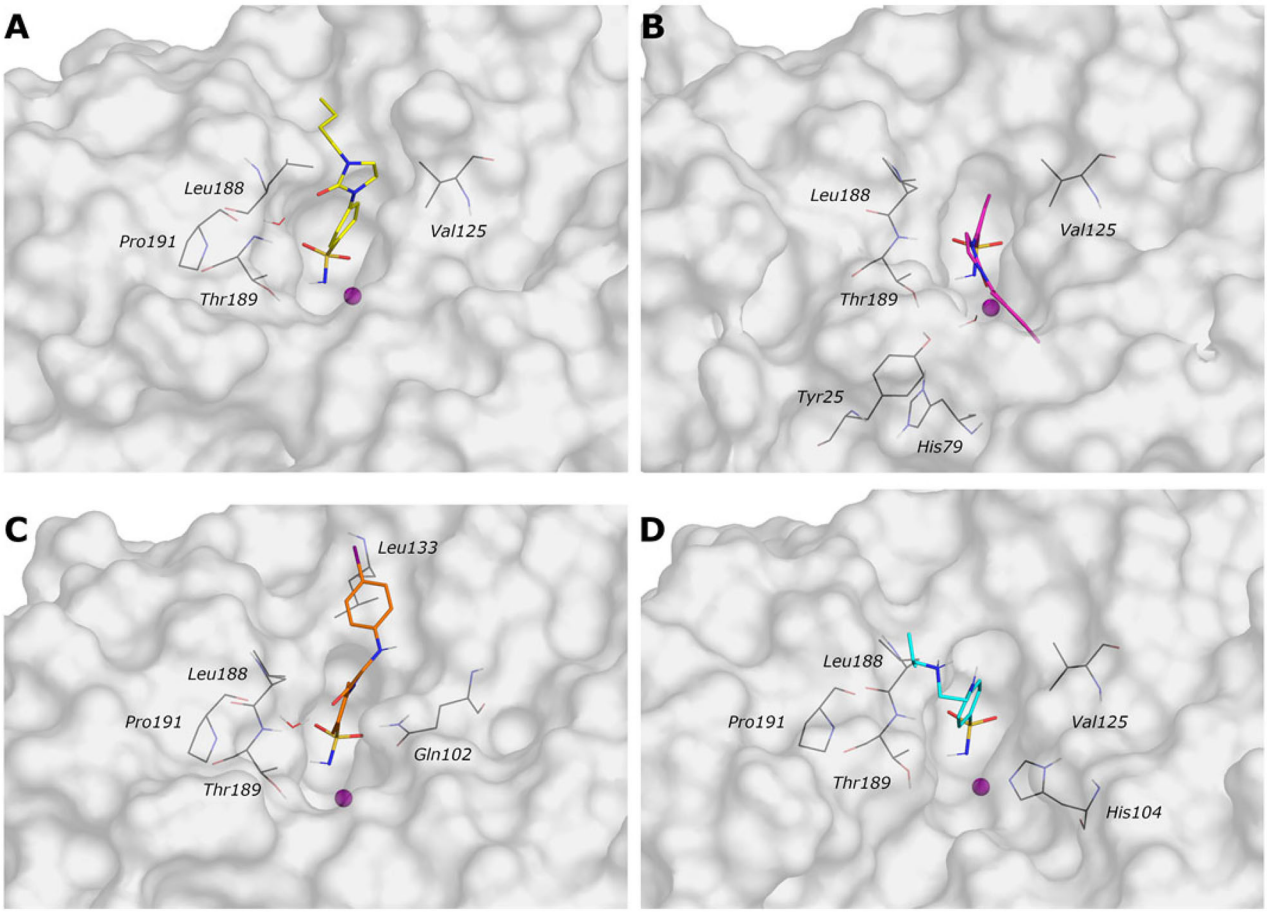

Figure 4. Most representative geometry retrieved after MD simulation for the four studied ligands. (A) **9c** yellow, (B) **12c** magenta, (C) **4b** orange, and (D) **10a** cyan in the *Vch*αCA (light grey). The compounds are represented in stick and the protein surface is visualised.

MD simulation analysis highlights the good stability of the studied complexes. The RMSD values calculated on the protein *Vch*αCA are relatively stable along the simulation and lower than 2.5 Å for all complexes. The same parameter calculated for ligands shows larger values, indicating a change in all ligands' initial binding conformation maintained along the production phase. The distal substituent to the benzene ring, exposed to the solvent, is the less stable part of the molecules during the simulation and is in charge of raising the RMSD value of the ligands as underlined by the RMSF values (Figures S1–S2 in Supporting Information). On the contrary, the benzenesulfonamide portion of all analysed ligands is firmly bound to the zinc ion and to Thr189 via a hydrogen bond. The most constrained compounds, **9c** (K_I = 4.7 nM) and **12c** (K_I = 11 nM), do not establish a π–π stacking contact with the zinc-coordinated His104 as for **4b** and **10a**, probably due to the steric hindrance of the 1,3-imidazolidin-2-one, but the carbonyl urea finds a water bridge interaction with Pro191 (Thr190) or Tyr25.

For ligand **9c** (Figure 4(A)), the protein average RMSD is close to 1.4 Å, whereas the ligand RMSD is 2.8 Å. During the simulation, the H-bond of the carbonyl urea with Gln102 is maintained at a very low percentage and is replaced by a water-bridged interaction with persistence of 22% (Figure 5(A)). The 1,3-imidazolidin-2-one turns in the opposite direction of Gln102 to find a water bridge interaction between the carbonyl oxygen and Pro191 (53%) or Thr190 (46%), confirming its conserved involvement in HB interactions even with different residues. Few hydrophobic interactions with residues of Val125, Leu133, and Leu188 are present in line with the docking study, and the *n*-butyl portion is exposed to the solvent (Figure 5(A,B)).

The analysis of the MD simulation of ligand **12c** (Figure 4(B)) reveals an average protein RMSD of 1.6 Å, whereas the average ligand RMSD is 2.6 Å. Similar to the previous inhibitor, the H-bond between the carbonyl group and Thr190 is maintained only for 20% of the simulation, while the 1,3-imidazolidin-2-one slightly turns to find a water bridge with Tyr25 (29%). The π-π stacking contact between the distal phenyl and Trp23 is similarly maintained for a very short time during the simulation, and it is replaced by a π-π stacking contact with His79 (20%, Figure 5(C,D)), following the rotation of the linker.

For ligand **4b** (Figure 4(C)), the average protein RMSD is 1.5 Å, whereas the ligand RMSD is 2.5 Å, with a significant fluctuation during the simulation caused mainly by the rotation of the 4-iodophenyl ring that flips between two different positions, as highlighted by the RMSD profile. As for the previous compounds, the benzenesulfonamide function coordinates the zinc ion, but there is also evidence of a π-π stacking between the benzene ring and His104 (27%). The carbonyl amide forms a water bridge interaction with Pro191 (36%) or Thr190 (24%), while the interaction with Gln102 is maintained for less than 20% of the production phase (Figure 5(E,F)), as for compound **9c**. The distal portion of the molecule is exposed to the solvent.

For the less restricted compound **10a** (Figure 4(D)), the protein average RMSD is 1.7 Å, whereas the ligand RMSD is 2.1 Å, with the

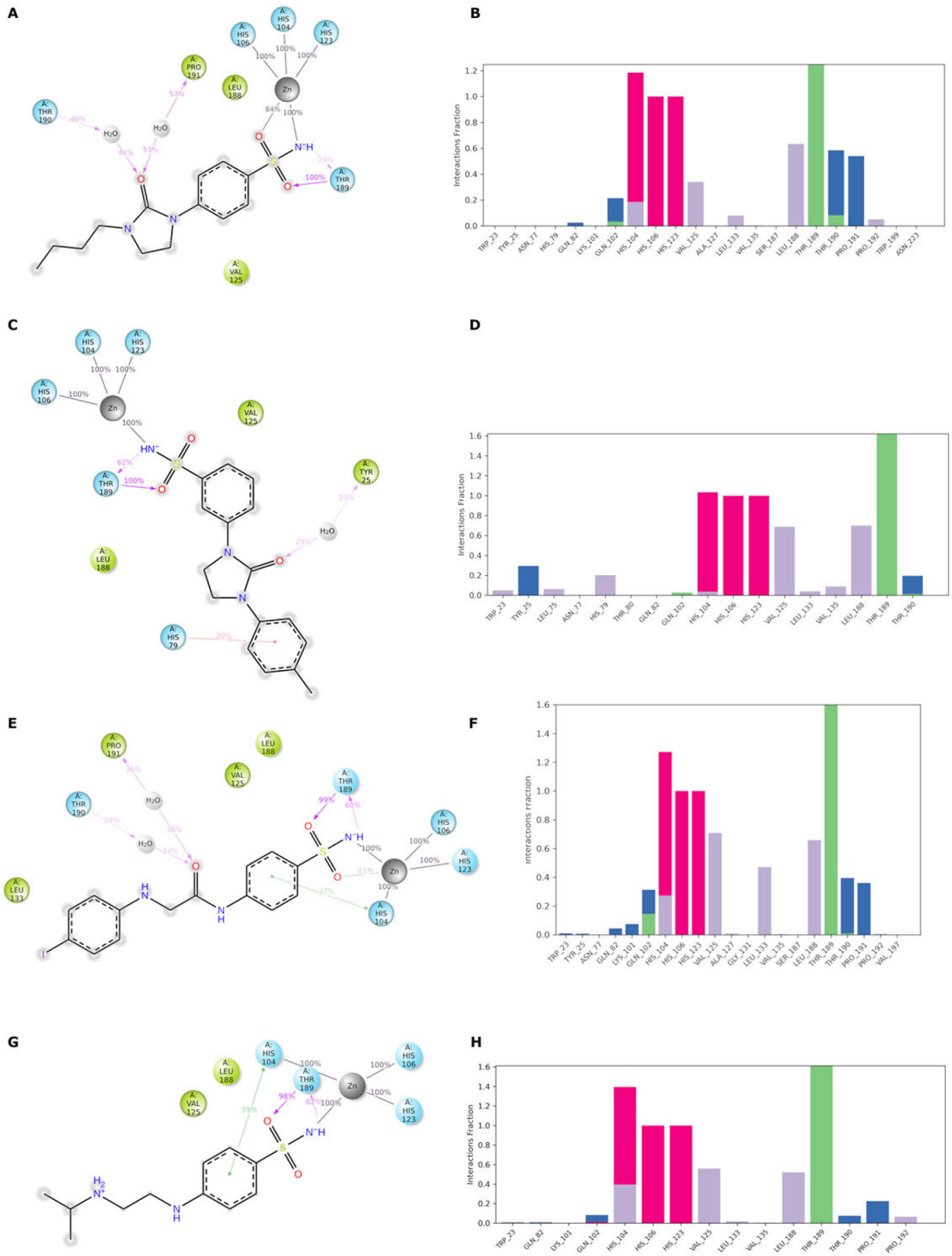

Figure 5. (A, C, E, and G) The 2D representation of most conserved ligand–protein interactions with (B, D, F, and H) the indication of the persistence (%) along the simulation and depiction of frequency and type of ligand-protein interaction along with the MD simulation. (A, B) **9c**, (C, D) **12c**, (E, F) **4b**, and (G, H) **10a**.

benzene sulfonamide substituent moving quite enough during the simulation. Other than the expected interactions of the sulfonamide with the zinc ion and Thr189, a π–π stacking contact between the benzene ring and His104 is present, also seen in the compound with the amide linker (**4b**). The interaction between the distal amine and Pro191 found in the docking study is maintained only for 20% of the simulation. The few hydrophobic interactions involve the residues Val125 and Leu188, whereas the

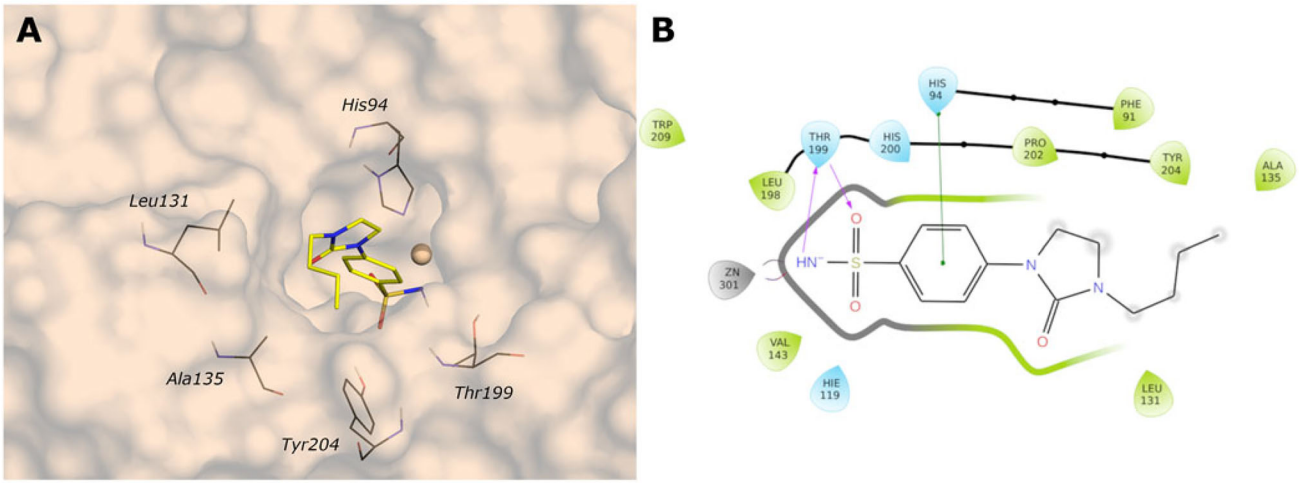

Figure 6. (A) Predicted 3D binding mode and (B) corresponding ligand interaction diagram of the most selective ligands **9c** (yellow) in the *h*CA I (light salon). The compound is represented as the stick and the protein surface is visualised.

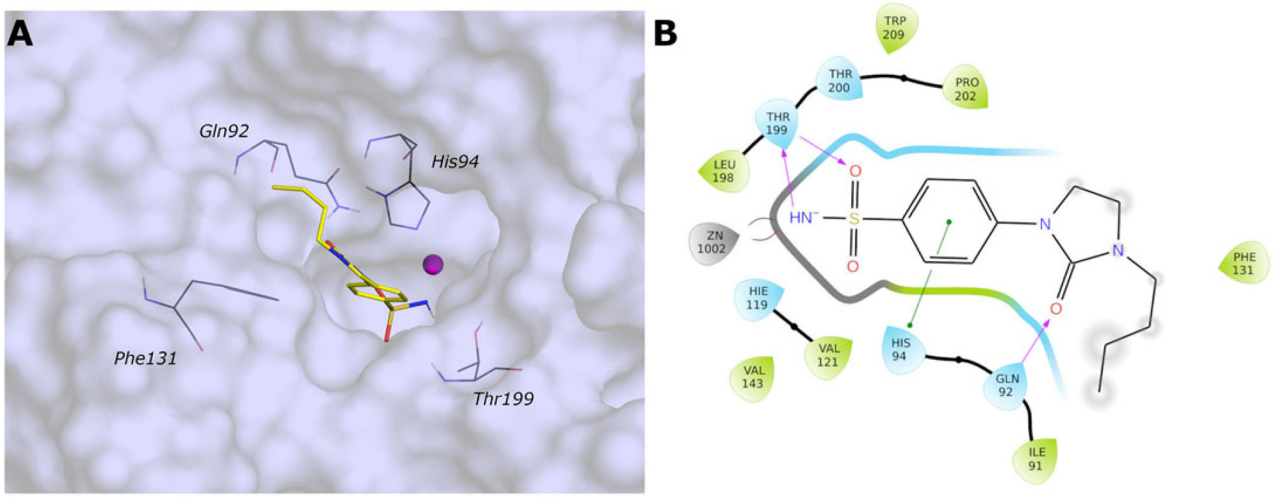

Figure 7. (A) Predicted 3D binding mode and (B) corresponding ligand interaction diagram of the most selective ligand **9c** (yellow) in the *h*CA II (light cyan). The compounds are represented as a stick and the protein surface is visualised.

linker and the isopropyl remain exposed to the solvent (Figure 5(G,H)).

Docking on the hCA I and hCA II

One of the current project's key aspects is the identification of compounds that selectively inhibit *Vch*CAs, sparing *h*CAs. To find out the critical features for the selectivity over, in particular, the *Vch*αCA, a docking protocol has been carried out on the human CA isoforms I and II (PDB ID: 6IOJ and 3K34, resolution 1.35 and 0.90 Å, respectively).

The analysis of the docking poses reveals that all compounds successfully adopt the correct geometry of the sulfonamide function that coordinates the zinc ion and a π–π stacking contact of the phenyl ring with His94 (*h*CA I and *h*CA II) for most compounds. As for *Vch*αCA, hydrophobic interactions are not prevalent, and the linker and the tail of most compounds are exposed to the solvent.

The active sites of hCA I and hCA II are superimposable to the active site of *Vch*αCA, except for the α-helix comprising residues 124–140 for *h*CA I and *h*CA II, which is much shorter in *Vch*αCA and forms a coil (residues 128–132)[49]. This determines a partial restriction at the edge of the active site of *h*CAs, causing a different placement of the inhibitor tail (Figures 6 and 7, Figures S3 and S4).

Docking on the VchβCA

Even if the activity of compounds results in the micromolar order on the *Vch*βCA, we investigated the binding mode of the studied compounds in the narrower active site of this isoform. Starting from the coordinates of the "closed" form of *Vch*βCA (PDB: 5CXK), the "open" form was generated by trimming the fundamental residue Asp^{A}44 during the Induced Fit protocol to obtain the conformational changes in the target sidechain that can resemble the "open" conformation of the *Vch*βCA. The obtained conformation of this residue was verified by overlapping the obtained protein with the crystal structure of the "open" β-CA of *Aspergillus fumigatus* (PDB: 7COJ). The coordinates of the cocrystallized **AAZ** in complex with β-CA of *Coccomyxa* (PDB: 3UCJ) were used to minimise the obtained "open" form of *Vch*βCA and optimise the residue positioning around the sulfonamide function. The minimised protein was then used to dock all ligands into the active site.

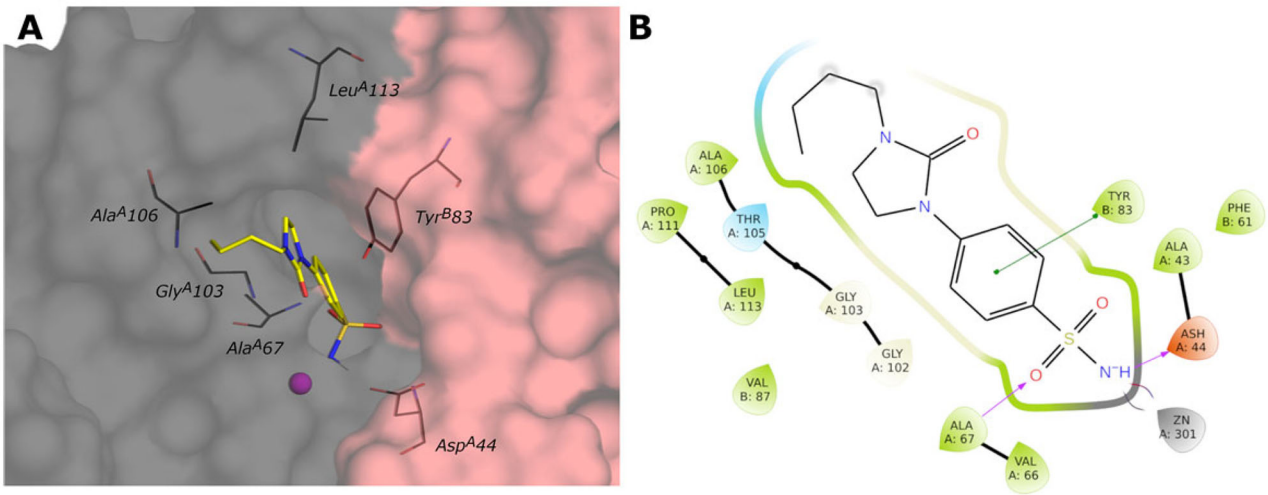

Figure 8. (A) Predicted 3D binding mode and (B) corresponding ligand interaction diagram of the most selective ligand **9c** (yellow) within *Vch*βCA (grey and pink). The compound is represented as a stick and the protein surface is visualised.

The docked poses of all compounds confirm that the sulfonamide group is coordinated and correctly oriented to the zinc ion, and the benzene ring interacts with Tyr^{B}83 by π–π stacking, reproducing the typical orientation of benzenesulfonamide inhibitors. Other fundamental contacts are with the hydrophobic pocket at chains A and B interface, involving Gly^{A}102, Gly^{A}103, Ala^{A}106, Pro^{A}113, and Leu^{A}113.

The docking results do not demonstrate different poses depending on the type of linker (amine, amide, or cyclic urea) or the *para* or *meta* position of the R-group. Even though the correct placement of the benzenesulfonamide group in the tight cleft of the *Vch*βCA, none of the compounds can establish more favourable interactions further than hydrophobic. The predicted binding mode and the ligand interactions of **9c** within the *Vch*βCA active site are represented in Figure 8.

*Docking on the Vch*γ*CA*

The 3D structure of *Vch*γCA was generated by homology modelling using the 3D crystal structure of γ-CA from *Escherichia coli* (PDB: 3TIO, identity 64.16%) as the template. The active site, located at the interface of two chains of the trimer of the *Vch*γCA, can exist in the "open" or "closed" conformation as already observed for the β isoform. The open form between chains D and F of 3TIO was chosen to model corresponding chains of the homologous *Vch*γCA. The 3D structure produced by homology modelling was compared with that predicted by AlphaFold2[48] and is available in the AlphaFold Protein Structure Database (https://alphafold.ebi.ac.uk/). Also in this case, the validity of our model was supported by the low RMSD value (0.772 Å) obtained by superimposing the two *Vch*γCA structures. As no benzenesulfonamide X-ray ligands are known to bind γ-CAs, we used the previously studied 4-(hydroxymethyl)benzenesulfonamide[31] as a reference to validate our model and optimise residues surrounding the sulfonamide portion. This compound was docked into *Vch*γCA, and the best-docked pose reveals the correct coordination geometry with the zinc ion, two H-bonds between the sulfonamide group and Gln^{F}61, the H-bond between the hydroxyl and Asp^{D}114, and hydrophobic interaction with Leu^{D}113, Met^{F}108, Leu^{F}105, Tyr^{F}168, similar to those previously obtained[31]. The complex of the best-docked pose of 4-(hydroxymethyl)benzenesulfonamide and the HM-*Vch*γCA was minimised to optimise residue positioning around the ligand. The obtained protein was then used to dock all compounds. The binding mode of all sulfonamide inhibitors in the active site replicates the interaction with zinc ion and Gln^{F}61. For compounds containing the amine linker (**1–15a**), the residue Asp^{D}114 is involved in an H-bond with the distal or proximal amine of ligands of the series *meta*- and *para*-substituted.

The *para*-substituted inhibitors with the amide linker (**1–15b**) deploy in the cylindrical active site interacting with the Met^{F}108 NH by the carbonyl group of the amide linker or with the carboxyl group of Asp^{D}114 by the NH of the amide. Only compound **15b** of the *meta*-substituted inhibitors interact with Asp^{D}114 with the amide and amine groups. The inhibitors characterised by the cyclic urea, in addition to the interactions of the sulfonamide group, engage only hydrophobic contacts with Leu^{F}105, Gly^{F}107, Met^{F}108, Leu^{F}141, Met^{F}143, Leu^{D}113, Pro^{D}132. Figure 9 shows the predicted binding mode and the ligand interactions of ligand **9c** within the *Vch*γCA active site.

In summary, the computational analysis suggests that the structural determinants contributing to ligand selectivity towards *Vch*αCA with respect to *h*CAs lie in the tail portion of arylsulfonamide ligands. Arylsulfonamides are well-known binders of αCAs, interacting with the zinc ion via the negatively charged NH^{-} group and establishing well-conserved H-bonds with a threonine residue. On the other hand, the rigidity of the linker increases the binding affinity towards all αCAs, both the human and bacterial isoenzymes. A more promising activity profile is accompanied by an H-bond acceptor in the rigid linker that directs the tail portion towards the *Vch*αCA coil (residues 128–134). The corresponding region in the human CAs is occupied by a short α-helix comprising residues 121–140 and constituting the most diverse region between human and bacterial αCAs (Figure 10).

Physicochemical and pharmacokinetic properties calculation

Parameters affecting the drug-likeness and bioavailability of the studied sulfonamides were predicted by using QikProp calculations[50] (Table S1 in Supporting Information).

Considering these compounds should act locally in the intestinal tract, we focussed on properties favouring their low

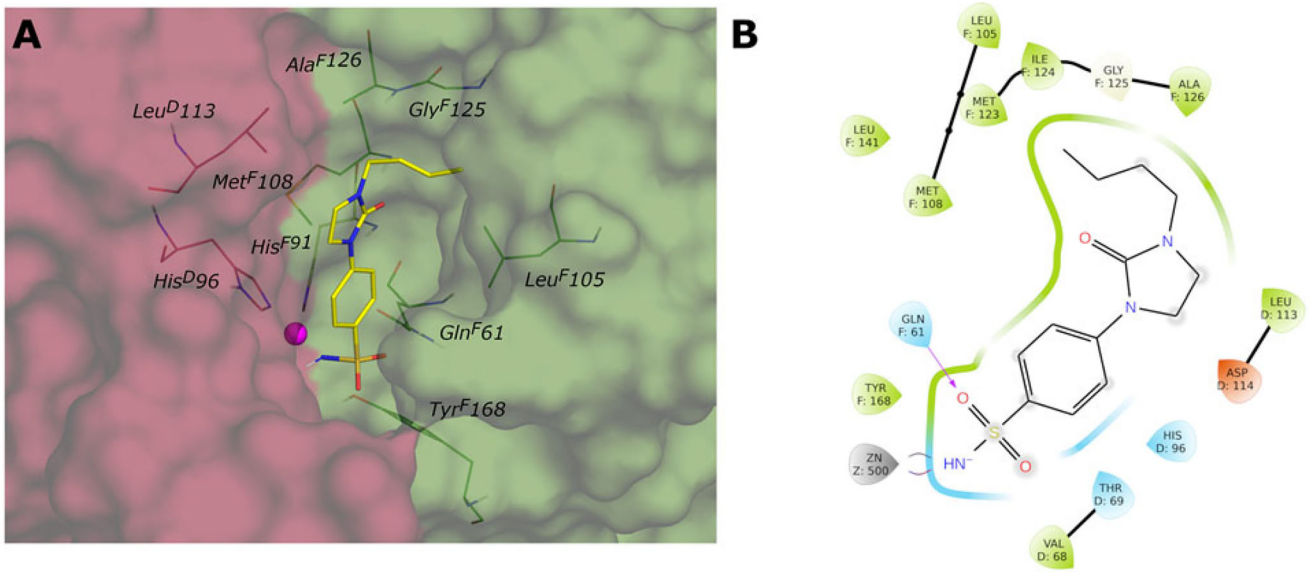

Figure 9. (A) Predicted 3D binding mode and (B) corresponding ligand interaction diagram of the most selective ligand **9c** (yellow) within *Vch*βCA (grey and pink). The compound is represented as a stick and the protein surface is visualised.

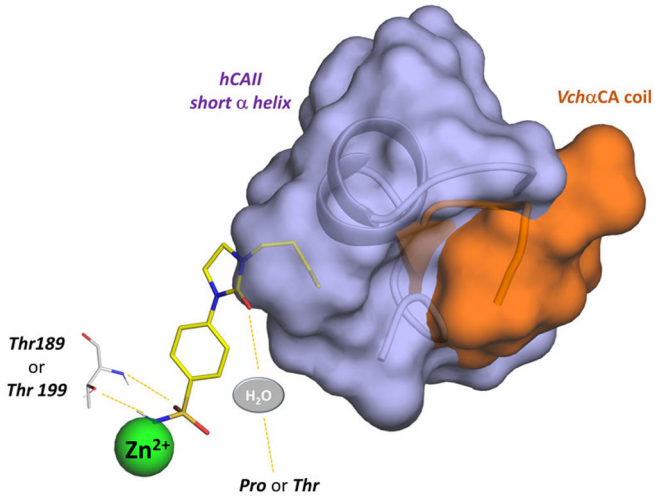

Figure 10. Schematic representation of the ligand contacts producing the selectivity towards *Vch*αCA with respect to *h*CAs. The compound (**9c**) is represented as sticks and the *Vch*αCA coil and the short alpha helix *h*CAII (similar to *h*CAI) are visualised as cartoon and surface.

Table 3. Physicochemical and pharmacokinetic properties of the studied ligands.

cpd	MW	PSA	Rule of Five	% *h* Oral Abs	QPP Caco	QP logBB	QP logHERG
9c	297.371	95.123	0	76.996	209.196	−1.454	−4.882
10a	257.35	89.372	0	60.538	67.277	−1.064	−5.688
12c	331.389	93.581	0	80.227	228.807	−1.242	−5.54
14b	384.247	111.98	0	72.068	134.213	−1.639	−6.072
AAZ	222.236	133.243	0	44.375	35.654	−1.802	−3.791

MW: molecular weight; PSA: Van der Waals surface area of polar nitrogen and oxygen atoms and carbonyl carbon atoms (7–200); Rule Of Five: Number of violations of Lipinski rule of five; *h* Oral Abs: human oral absorption (1, 2, or 3 for low, medium, or high); % *h* OralAbs: Predicted human oral absorption on a 0–100% scale; QPPCaco: Predicted apparent Caco-2 cell permeability in nm/s. Caco-2 cells are a model for the gut–blood barrier (500 great); QPlogBB: Predicted brain/blood partition coefficient (−3.0 to 1.2); QPlogHERG: Predicted IC_{50} value for the blockage of HERG K^+ channels (concern below −5).

absorption. It is known from the literature that compounds working locally in the gut[51] are usually polar, with a high molecular weight (MW) and polar surface area (PSA). In this case, focussing on the most selective inhibitors, it is possible to highlight their compliance with Lipinski's Rule of five, their limited permeability of the gut–blood barrier, and the blood-brain barrier (BBB). Some concerns are due to the possible binding to HERG. Table 3 shows the essential properties for the most selective compounds.

Direct-acting antibacterial activity

Most of the compounds (**1a**, **2c**, **3a–c**, **4–5c**, **6b–c**, **7c**, **8–9a–c**, **10c**, **11a–c**, **12c**, **13a–c**, **14a**, **15a**) and **AAZ** were tested on three different clinical isolates of *V. cholerae*, namely SI-Vc22, SI-Vc71, and SI-Vc912, to assess their direct antibacterial activity. Using an agar diffusion method (ampicillin, chloramphenicol, and ciprofloxacin were used as reference antibiotics), only twelve (amines **8–9a**, **11a**, and **13a**, amides **3b**, **9b,** and **11b**, ureas **4–7c** and **9c**) out of 28 tested compounds showed a moderate growth inhibition against at least one of the clinical isolates. Five compounds (amines **9a**, **11a,** and ureas **4c**, **6c**, **9c**) were found to be moderately active on all the isolates (inhibition zone diameter in the range of 3–5 mm; data not shown).

However, the determination of the minimum inhibitory concentrations (MICs) (broth microdilution method) confirmed the very low direct-acting activity of these compounds, as MIC values were ≥64 μg/mL. These data are not entirely unexpected considering that the inhibition of *Vch*CAs would not result to be to be detrimental for the bacterium *in vitro*, but would be important *in vivo*, especially for the onset of virulence, whose study would require far more complicated biological investigations. However, and since we can now confirm the lack of a direct antibacterial activity for all the derivatives, it would be extremely interesting to assess whether these compounds could inhibit the production of the active exotoxin (e.g. with gene reporting, biochemical or cellular assays) to verify this hypothesis[52].

Conclusions

Herein, we reported the design strategy of CA inhibitors bearing conformationally restricted alkyl/aryl amines and amides into imidazolidinones. These *para*- or *meta*-benzenesulfonamides are *ad hoc* characterised by differential rotational features, leading to highly potent (nanomolar) and selective compounds acting preferentially against *Vch*αCA with respect to β- and γ-isoforms.

Stopped flow-based enzymatic assays showed that all the compounds, with properly *inter*-series differences, are able to strongly inhibit *Vch*αCA, with the following progressive inhibitory potency: *meta*-benzenesulfonamides < *para*-benzenesulfonamides and amine < amide < cyclic urea.

Although the above-mentioned trend was not completely respected and it resulted to be quite different for some substituents, we could notice that the more the linker is rigid (urea) the more the inhibition is strong. Thus, by performing these preliminary SAR considerations, we could assume that the activity profile of the derivatives library is strictly linked to the different rigidity of the compounds tail. After a preliminary calculation of the flexibility properties of representative compounds, we find out how they affect the affinity of the whole set of compounds for the different enzyme catalytic sites and, thereby, their inhibitory activities. In particular, we investigated their binding poses in both the human and bacterial enzymes through an in-depth structure-based computational study. Moreover, MD simulations of the most selective inhibitors of *Vch*αCA revealed the high stability of the benzenesulfonamide core in the interaction with the zinc ion, assuming the usual coordination geometry. The structural determinants able to guarantee a proper interaction with the active site were found to be (i) the presence of the urea carbonyl group in the linker (**9c**), able to establish a water-mediated hydrogen bond with Pro191 or Thr190, and (ii) the constraint of the linker in cyclic urea, producing the highest selectivity over the *h*CA I and II.

In silico, ADME was also investigated to assess the physicochemical properties of the benzenesulfonamide derivatives and the compounds were found to be in accordance with Lipinski's rule, even if they seem to suffer from a low oral bioavailability. Keeping into consideration the localisation of our target, this property can be considered fruitful to avoid systemic distribution and off-target interaction.

Although not entirely unexpected, antibacterial susceptibility assays on three different epidemiologically unrelated *V. cholerae* strains confirmed the lack of direct-acting antibacterial activity of these compounds. Further characterisation of these compounds would be required to evaluate their potential inhibition of the production of virulence determinants, of primary importance in the host environment, although this study is beyond the scope of the present work.

In summary, a combined analysis of inhibitory enzymatic activity and *in silico* simulations of a large library of benzenesulfonamide derivatives revealed and rationalised specific SARs regarding the rigidity/flexibility properties of the compounds tail. Thus, thanks to our protocol, we screened 45 benzenesulfonamides decorated with three different moieties (amine, amide, and cyclic urea) and a number of decorated tails against the three CA expressed by *V. cholerae* pathogen though the versatile and high-throughput stopped-flow technique. The obtained K_I values highlighted interesting activity profile for several derivatives and notable isoform selectivity was found for at least one compound for series, such as the 4-benzenesulfonamides with amino (**10a**), amido (**4b**), and the cyclic urea (**9c**) moieties and only one 3-benzenesulfonamide derivative (**12c**).

Further efforts will be focussed on the assessment of the antibacterial behaviour of these compounds in an infection model to evaluate their activity towards the virulence and pathogenicity of the bacterium.

Material and methods

Preparation of the derivative libraries

The compounds were prepared as reported according to the general synthetic approach reported in Scheme 1[40].

In vitro carbonic anhydrase inhibition assay

The CA-catalyzed CO_2 hydration activity was performed on an Applied Photophysics stopped-flow instrument using Phenol Red, at a concentration of 0.2 mM, as a pH indicator working at the maximum absorbance of 557 nm[53,54] with 20 mM HEPES (pH 7.40 for α- and 8.40 for β-CAs and γ-CAs) as the buffer, 20 mM Na_2SO_4 to maintain constant ionic strength, and following the initial rates of the CA-catalyzed CO_2 hydration reaction for a period of 10 − 100 s and The CO_2 concentrations ranged from 1.7 to 17 mM for the determination of the kinetic parameters and inhibition constants. Enzyme concentrations ranged between 5 and 12 nM. For each inhibitor, at least six traces of the initial 5 − 10% of the reaction have been used to determine the initial velocity. The uncatalyzed reaction rates were determined in the same manner and subtracted from the total observed rates. Stock solutions of inhibitor (0.1 mM) were prepared in distilled-deionized water, and dilutions up to 0.01 nM were prepared. Solutions containing inhibitor and enzyme were preincubated for 15 min at room temperature prior to performing the assay to allow the formation of the E − I complex. The inhibition constants were obtained by non-linear least-squares methods using PRISM 3[29] and the Cheng-Prusoff equation as reported earlier and represent the mean from at least three different determinations. All CA isoforms are recombinant and obtained *in-house*, as reported earlier[29].

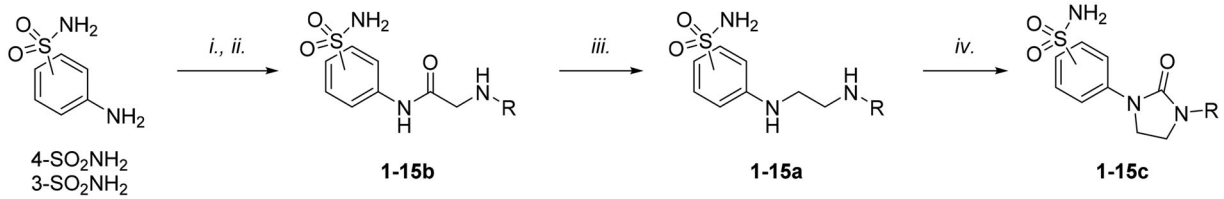

Scheme 1. Synthesis of compounds **1-15a–c**. Reagents and conditions: (i) chloroacetyl chloride, dry acetone, N_2, 0 °C, 0.5 h; (ii) appropriately substituted aniline, KI, sealed tube, dry THF, N_2, 110 °C, 24 h; or 2-amino-6-methylpyridine, dry TEA, abs EtOH, N_2, ref., 24 h; or benzylamine, dry TEA, dry ACN, N_2, 24 h; or amine, KI, dry THF, N_2, 24 h; (iii) 1 M BH3·THF, dry THF, N_2, r.t., 24 h; or $LiAlH_4$, dry THF, N_2, 0–70 °C, 24 h; (iv). triphosgene, dry TEA, dry THF, N_2, r.t., 2 h.

In silico studies

Calculation of flexibility properties of the derivatives

Flexibility and numbers of rotable/rigid bonds were calculated through FAFDrugs4 (Free ADME-Tox Filtering Tool)[46].

3D protein structure retrieval

Molecular modelling studies were performed on Schrödinger Life-Sciences Suite 2021–4[50]. All ligands were drawn as 2D structures from Maestro and prepared by using LigPrep to generate the 3D geometry and find all possible tautomers and protonation states at pH 7.0 ± 0.4 with Epik[55,56]. The three-dimensional X-ray structures of *h*CA I and *h*CA II were retrieved from the Protein Data Bank (PDB ID: 6IOJ and 3K34, resolution 1.35 and 0.90 Å, respectively)[57,58]. The Protein Preparation workflow was used to correct, optimise and minimise the crystal structures. The crystal structure of *Vch*βCA was retrieved from the Protein Data Bank (PDB ID: 5CXK, resolution 1.90 Å)[59]. The "open" catalytic site of *Vch*βCA was realised starting from the crystallographic "closed" form of the crystal structure. The Induced-fit protocol[60–62] was used by employing Glide[63–65] and Prime[66,67] software with the OLPS4 force field, and the fundamental residue Asp^{A}44 was trimmed to obtain the conformational changes in the target sidechain that can resemble the "open" conformation of the *Vch*βCA. The resulting conformation of the Asp^{A}44 side chain was checked by overlapping it to the "open" *Vch*βCA of the fungal pathogen *Aspergillus fumigatus* (PDB: 7COJ)[68].

Homology modelling

The 3D structures of *Vch*αCA and *Vch*γCA were obtained by homology modelling. The primary sequences of *Vch*αCA (Uniprot ID: A0A0H6VI20, 249 aa) and *VCh*γCA (Uniprot ID: A0A0H6TVJ0, 184 aa) were retrieved from the UniProt KnowledgeBase (UniProtKB) database[69]. The protein sequence was used as a query sequence for homology modelling using Prime. This tool used BLAST[70] to identify suitable templates from Protein Data Bank (PDB) using a single template protocol. The homology models of *Vch*αCA and *Vch*γCA were obtained on the structure of αCA from *Photobacterium profundus* (PDB: 5HPJ, identity 64.75%) and the structure of γ-CA from *Escherichia coli* γCA (PDB: 3TIO, identity 64.16%) as the template, respectively[71,72]. For *Vch*γCA, the chains D-F were used as the template as they present the catalytic site in the "open" form. The crystallographic **AAZ** ligand coordinates taken from the complex with *Helicobacter pylori* αCA (PDB: 4YGF) and the 4-(hydroxymethyl)benzenesulfonamide[31] were added as ligands to the homology models of α and γ isoforms, respectively. The protein-ligand complexes were fully minimised by using MacroModel applying the OPLS4 force field, 5000 steps of PRCG minimisation algorithm with a convergence criterion of 0.05 KJ/mol Å, to optimise the residue positioning around the sulfonamide function.

Docking calculations

Molecular docking analyses were performed using the Glide software. The Glide Grids were generated by positioning the enclosing boxes on the centre of mass of the respective sulfonamide ligands. The SP docking protocol was used by setting 5000 poses per ligand for the initial phase and 400 poses per ligand for energy minimisation with the OPLS4 forcefield. Rotatable groups were defined for each protein: Thr189 for *Vch*αCA, Asp^{A}44 for *Vch*βCA, Thr^{D}69 for *Vch*γCA, and Thr199 for *h*CAs. Additionally, a core constraint on the sulfonamide positioning was applied in the docking protocol into the *Vch*αCA and *Vch*βCA.

Molecular Dynamics

Molecular Dynamics simulation was carried out using Desmond[50,73]. The complexes of *Vch*αCA with the docked poses of compounds **9c**, **12c**, **4b**, and **10a** were embedded in an orthorhombic box of TIP4P water molecules resulting in systems of 28 787, 28 824, 28 748, 28 840 atoms, respectively. In order to balance the system charge, sodium, and chlorine ions were added. The systems were relaxed by applying the default relaxation protocol before the production phase. The simulation duration was set to 100 ns registering frames every 100 ps. The OPLS4 force field, a normal pressure-temperature (NPT) ensemble with a Nose–Hoover thermostat set to 300 K and a Martyna–Tobias–Klein barostat set to 1.01325 bar pressure were used. Electrostatic interactions were examined by applying the smooth particle mesh Ewald method. Figures were generated using Maestro and PyMoL[74].

QikProp calculations

Physico-chemical and pharmacokinetic parameters were calculated using QikProp[50] and applying the default parameters.

Antibacterial susceptibility testing

Epidemiologically unrelated clinical isolates of *V. cholerae* (SI-Vc22, SI-Vc71, and SI-Vc-912) were obtained from the collection of the Department of Medical Biotechnologies (University of Siena, Italy). Compounds were resuspended in DMSO at a final concentration of 50 mg/mL. For insoluble compounds, DMSO was further added to lower the concentration until complete solubility of the compound (final concentrations, 25, 12.5, or 6.25 mg/mL). The direct antibacterial activity was evaluated using an agar diffusion-based method[75]. Briefly, Mueller-Hinton agar plates were inoculated with a bacterial suspension containing $\approx 1.5 \times 10^8$ CFU/mL of the tested strain. 2 μL of each compound solution were spotted on the surface of the inoculated medium and incubated at 37 °C for 24 h. Controls included the vehicle (100% DMSO) or 2-μL spots of an antibiotic (ampicillin, chloramphenicol and ciprofloxacin) solution in sterile milliQ water (5 mg/mL, *i.e.* each spot contained 10 μg of the antibiotic). The results were recorded as the diameter of the growth inhibition zone.

MIC values of the compounds were determined using the broth microdilution method as recommended by Clinical Laboratory Standards Institute[76]. Bacterial inoculum was 5×10^4 CFU/well. MICs were recorded after 18 h of incubation at 35 °C.

Acknowledgements

This research was partially supported by the Italian Ministry for University and Research (MIUR) grant number FISR2019_04819 BacCAD to S.C., C.C., and C.T.S. This work (J.D.D.) was supported also in part by the Italian MUR (Ministero dell'Università e Ricerca) in the frame of the PNRR PE-13 ("Piano Nazionale di Ripresa e Resilienza, Partenariato Esteso 13, Malattie infettive emergenti") INF-ACT project (One Health Basic and Translational Research Actions addressing Unmet Needs on Emerging Infectious Diseases). Thanks are due to Dr. Stefania Cresti (Department of Medical Biotechnologies, University of Siena & Azienda Ospedaliero- Universitaria Senese, Siena, Italy) and to Tiziana Di

Maggio and Prof. Lucia Pallecchi (Department of Medical Biotechnologies, University of Siena, Italy) and Prof. Gian Maria Rossolini (Department of Experimental and Clinical Medicine, University of Florence, Florence, Italy; Clinical Microbiology and Virology Unit, Careggi University Hospital, Florence, Italy) for providing the bacterial strains used in this work.

Authors contributions

The manuscript was written through the contributions of all authors. All authors approved the final version of the manuscript.

Disclosure statement

C.T. Supuran is Editor-in-Chief of the Journal of Enzyme Inhibition and Medicinal Chemistry. He was not involved in the assessment, peer review, or decision-making process of this paper. The authors have no relevant affiliations or financial involvement with any organisation or entity with a financial interest in or financial conflict with the subject matter or materials discussed in the manuscript.

Funding

This work was supported by Ministero dell'Istruzione, dell'Università e della Ricerca [FISR2019_04819].

ORCID

Marialuigia Fantacuzzi http://orcid.org/0000-0003-2401-7547
Ilaria D'Agostino http://orcid.org/0000-0002-4870-7326
Simone Carradori http://orcid.org/0000-0002-8698-9440
Fabrizio Carta http://orcid.org/0000-0002-1141-6146
Mariangela Agamennone http://orcid.org/0000-0001-5198-0051
Andrea Angeli http://orcid.org/0000-0002-1470-7192
Filomena Sannio http://orcid.org/0000-0003-3001-8159
Jean-Denis Docquier http://orcid.org/0000-0001-9483-4476
Clemente Capasso http://orcid.org/0000-0003-3314-2411
Claudiu T. Supuran http://orcid.org/0000-0003-4262-0323

References

1. Silva DL, Lima CM, Magalhães VCR, Baltazar LM, Peres NTA, Caligiorne RB, Moura AS, Fereguetti T, Martins JC, Rabelo LF, et al. Fungal and bacterial coinfections increase mortality of severely ill COVID-19 patients. J Hosp Infect. 2021;113:145–154.
2. Bardet A, Fraslin AM, Marghadi J, Borget I, Faron M, Honoré C, Delaloge S, Albiges L, Planchard D, Ducreux M, et al. Impact of COVID-19 on healthcare organisation and cancer outcomes. Eur J Cancer. 2021;153:123–132.
3. Uwishema O, Okereke M, Onyeaka H, Hasan MM, Donatus D, Martin Z, Oluwatomisin LA, Mhanna M, Olumide AO, Sun J, et al. Threats and outbreaks of cholera in Africa amidst COVID-19 pandemic: a double burden on Africa's health systems. Trop Med Health. 2021;49(1):93.
4. D'Mello-Guyett L, Gallandat K, Van den Bergh R, Taylor D, Bulit G, Legros D, Maes P, Checchi F, Cumming O. Prevention and control of cholera with household and community water, sanitation and hygiene (WASH) interventions: A scoping review of current international guidelines. PLOS One. 2020;15(1):e0226549.
5. WHO. [accessed 2023 Jan 31]. https://www.who.int/news-room/fact-sheets/detail/cholera.
6. ECDC. [accessed 2023 Jan 31]. https://www.ecdc.europa.eu/en/all-topics-z/cholera/surveillance-and-disease-data/cholera-monthly.
7. Owoicho O, Abechi P, Olwal CO. Cholera in the era of COVID-19 pandemic: a worrying trend in Africa? Int J Public Health. 2021;66:1604030.
8. Oladapo RK, Oyetola AB, Obidiro OP, Olajide A, Osuagwu-Nwogu E, Olaitan OM, Ngokere C, Monisola I, Ibraheem B, Afolayan A. Rising cholera cases: harnessing the momentum of COVID-19 to strengthen Nigeria's health systems. Int J Health Plann Manage. 2021;36(6):2030–2034.
9. Faruque SM, Ahmed KM, Siddique AK, Zaman K, Alim AR, Albert MJ. Molecular analysis of toxigenic *Vibrio cholerae* O139 Bengal strains isolated in Bangladesh between 1993 and 1996: evidence for emergence of a new clone of the Bengal vibrios. J Clin Microbiol. 1997;35(9):2299–2306.
10. CDC. [accessed 2023 Jan 31]. https://www.cdc.gov/cholera/treatment/antibiotic-treatment.html. (accessed on 31/01/2023).
11. Das B, Verma J, Kumar P, Ghosh A, Ramamurthy T. Antibiotic resistance in *Vibrio cholerae*: understanding the ecology of resistance genes and mechanisms. Vaccine. 2020;38(Suppl 1):A83–A92.
12. Ahmadi MH. Global status of tetracycline resistance among clinical isolates of *Vibrio cholerae*: a systematic review and meta-analysis. Antimicrob Resist Infect Control. 2021;10(1):115.
13. Gupta P, Modgil V, Kant V, Kaur H, Narayan C, Mahindroo J, Verma R, Mohan B, Taneja N. Phenotypic and genotypic characterization of antimicrobial resistance in clinical isolates of *Vibrio cholerae* over a decade (2002–2016). Indian J Med Microbiol. 2022;40(1):24–29.
14. Mashe T, Domman D, Tarupiwa A, Manangazira P, Phiri I, Masunda K, Chonzi P, Njamkepo E, Ramudzulu M, Mtapuri-Zinyowera S, et al. Highly resistant cholera outbreak strain in Zimbabwe. N Engl J Med. 2020;383(7):687–689.
15. Campestre C, De Luca V, Carradori S, Grande R, Carginale V, Scaloni A, Supuran CT, Capasso C. Carbonic anhydrases: new perspectives on protein functional role and inhibition in *Helicobacter pylori*. Front Microbiol. 2021;12:629163.
16. Supuran CT. Structure and function of carbonic anhydrases. Biochem J. 2016;473(14):2023–2032.
17. De Luca V, Carginale V, Supuran CT, Capasso C. gram-negative bacterium *Escherichia coli* as a model for testing the effect of carbonic anhydrase inhibition on bacterial growth. J Enzyme Inhib Med Chem. 2022;37(1):2092–2098.
18. Hewitt CS, Abutaleb NS, Elhassanny AEM, Nocentini A, Cao X, Amos DP, Youse MS, Holly KJ, Marapaka AK, An AW, et al. Structure-activity relationship studies of acetazolamide-based carbonic anhydrase inhibitors with activity against *Neisseria gonorrhoeae*. ACS Infect Dis. 2021;7(7):1969–1984.
19. Abutaleb NS, Elkashif A, Flaherty DP, Seleem MN. *In Vivo* antibacterial activity of acetazolamide. Antimicrob Agents Chemother. 2021;65(4):e01715-e01720.
20. Kaur J, Cao X, Abutaleb NS, Elkashif A, Graboski AL, Krabill AD, AbdelKhalek AH, An W, Bhardwaj A, Seleem MN, et al. Optimization of acetazolamide-based scaffold as potent inhibitors of vancomycin-resistant *Enterococcus*. J Med Chem. 2020;63(17):9540–9562.
21. Abutaleb NS, Elhassanny AEM, Flaherty DP, Seleem MN. *In vitro* and *in vivo* activities of the carbonic anhydrase

inhibitor, dorzolamide, against vancomycin-resistant enterococci. Peer J. 2021;9:e11059.
22. Abutaleb NS, Elhassanny AEM, Seleem MN. In vivo efficacy of acetazolamide in a mouse model of *Neisseria gonorrhoeae* infection. Microb Pathog. 2022;164:105454.
23. Mancuso F, De Luca L, Bucolo F, Vrabel M, Angeli A, Capasso C, Supuran CT, Gitto R. 4-sulfamoylphenylalkylamides as inhibitors of carbonic anhydrases expressed in *Vibrio cholerae*. ChemMedChem. 2021;16(24):3787–3794.
24. Akgul O, Angeli A, Selleri S, Capasso C, Supuran CT, Carta F. Taurultams incorporating arylsulfonamide: first in vitro inhibition studies of α-, β- and γ-class Carbonic Anhydrases from *Vibrio cholerae* and *Burkholderia pseudomallei*. Eur J Med Chem. 2021;219:113444.
25. Abuaita BH, Withey JH. Bicarbonate Induces *Vibrio cholerae* virulence gene expression by enhancing ToxT activity. Infect Immun. 2009;77(9):4111–4120.
26. Butler SM, Camilli A. Going against the grain: chemotaxis and infection in *Vibrio cholerae*. Nat Rev Microbiol. 2005;3(8):611–620.
27. Szklarczyk D, Gable AL, Nastou KC, Lyon D, Kirsch R, Pyysalo S, Doncheva NT, Legeay M, Fang T, Bork P, et al. The STRING database in 2021: customizable protein-protein networks, and functional characterization of user-uploaded gene/measurement sets. Nucleic Acids Res. 2021;49(D1):D605–D612.
28. Zeller T, Klug G. Thioredoxins in bacteria: functions in oxidative stress response and regulation of thioredoxin genes. Naturwissenschaften. 2006;93(6):259–266.
29. Del Prete S, De Luca V, Scozzafava A, Carginale V, Supuran CT, Capasso C. Biochemical properties of a new α-carbonic anhydrase from the human pathogenic bacterium, *Vibrio cholerae*. J Enzyme Inhib Med Chem. 2014;29(1):23–27.
30. Del Prete S, Vullo D, De Luca V, Carginale V, Osman SM, AlOthman Z, Supuran CT, Capasso C. Comparison of the sulfonamide inhibition profiles of the α-, β- and γ-carbonic anhydrases from the pathogenic bacterium *Vibrio cholerae*. Bioorg Med Chem Lett. 2016;26(8):1941–1946.
31. Bonardi A, Nocentini A, Osman SM, Alasmary FA, Almutairi TM, Abdullah DS, Gratteri P, Supuran CT. Inhibition of α-, β- and γ-carbonic anhydrases from the pathogenic bacterium *Vibrio cholerae* with aromatic sulphonamides and clinically licenced drugs – a joint docking/molecular dynamics study. J Enzyme Inhib Med Chem. 2021;36(1):469–479.
32. Bonardi A, Nocentini A, Cadoni R, Del Prete S, Dumy P, Capasso C, Gratteri P, Supuran CT, Winum JY. Benzoxaboroles: new potent inhibitors of the carbonic anhydrases of the pathogenic bacterium *Vibrio cholerae*. ACS Med Chem Lett. 2020;11(11):2277–2284.
33. Demir-Yazıcı K, Güzel-Akdemir Ö, Angeli A, Supuran CT, Akdemir A. Novel indole-based hydrazones as potent inhibitors of the α-class carbonic anhydrase from pathogenic bacterium *Vibrio cholerae*. IJMS. 2020;21(9):3131.
34. Bua S, Berrino E, Del Prete S, Murthy VS, Vijayakumar V, Tamboli Y, Capasso C, Cerbai E, Mugelli A, Carta F, et al. Synthesis of novel benzenesulfamide derivatives with inhibitory activity against human cytosolic carbonic anhydrase I and II and *Vibrio cholerae* α- and β-class enzymes. J Enzyme Inhib Med Chem. 2018;33(1):1125–1136.
35. Berrino E, Bozdag M, Del Prete S, Alasmary FAS, Alqahtani LS, AlOthman Z, Capasso C, Supuran CT. Inhibition of α-, β-, γ-, and δ-carbonic anhydrases from bacteria and diatoms with N'-aryl-N-hydroxy-ureas. J Enzyme Inhib Med Chem. 2018;33(1):1194–1198.
36. Ali M, Angeli A, Bozdag M, Carta F, Capasso C, Farooq U, Supuran CT. Benzylaminoethylureido-tailed benzenesulfonamides show potent inhibitory activity against bacterial carbonic anhydrases. ChemMedChem. 2020;15(24):2444–2447.
37. Ceruso M, Del Prete S, Alothman Z, Capasso C, Supuran CT. Sulfonamides with potent inhibitory action and selectivity against the α-carbonic anhydrase from *Vibrio cholerae*. ACS Med Chem Lett. 2014;5(7):826–830.
38. De Vita D, Angeli A, Pandolfi F, Bortolami M, Costi R, Di Santo R, Suffredini E, Ceruso M, Del Prete S, Capasso C, et al. Inhibition of the α-carbonic anhydrase from *Vibrio cholerae* with amides and sulfonamides incorporating imidazole moieties. J Enzyme Inhib Med Chem. 2017;32(1):798–804.
39. Mancuso F, De Luca L, Angeli A, Berrino E, Del Prete S, Capasso C, Supuran CT, Gitto R. In silico-guided identification of new potent inhibitors of carbonic anhydrases expressed in *Vibrio cholerae*. ACS Med Chem Lett. 2020;11(11):2294–2299.
40. Liguori F, Carradori S, Ronca R, Rezzola S, Filiberti S, Carta F, Turati M, Supuran CT. Benzenesulfonamides with different rigidity-conferring linkers as carbonic anhydrase inhibitors: an insight into the antiproliferative effect on glioblastoma, pancreatic, and breast cancer cells. J Enzyme Inhib Med Chem. 2022;37(1):1857–1869.
41. Combs J, Bozdag M, Cravey LD, Kota A, McKenna R, Angeli A, Carta F, Supuran CT. New insights into conformationally restricted carbonic anhydrase inhibitors. Molecules. 2023;28(2):890.
42. Scozzafava A, Menabuoni L, Mincione F, Briganti F, Mincione G, Supuran CT. Carbonic anhydrase inhibitors. Synthesis of water-soluble, topically effective, intraocular pressure-lowering aromatic/heterocyclic sulfonamides containing cationic or anionic moieties: Is the tail more important than the ring? J Med Chem. 1999;42(14):2641–2650.
43. Bozdag M, Ferraroni M, Nuti E, Vullo D, Rossello A, Carta F, Scozzafava A, Supuran CT. Combining the tail and the ring approaches for obtaining potent and isoform-selective carbonic anhydrase inhibitors: solution and X-ray crystallographic studies. Bioorg Med Chem. 2014;22(1):334–340.
44. Wilkinson BL, Bornaghi LF, Houston TA, Innocenti A, Supuran CT, Poulsen S-A. A novel class of carbonic anhydrase inhibitors: glycoconjugate benzene sulfonamides prepared by "click-tailing. J Med Chem. 2006;49(22):6539–6548.
45. Khalifah RG. The carbon dioxide hydration activity of carbonic anhydrase. I. Stop-flow kinetic studies on the native human isoenzymes B and C. J Biol Chem. 1971;246(8):2561–2573.
46. Lagorce D, Bouslama L, Becot J, Miteva MA, Villoutreix BO. FAF-drugs4: free ADME-tox filtering computations for chemical biology and early stages drug discovery. Bioinformatics. 2017;33(22):3658–3660.
47. Veber DF, Johnson SR, Cheng HY, Smith BR, Ward KW, Kopple KD. Molecular properties that influence the oral bioavailability of drug candidates. J Med Chem. 2002;45(12):2615–2623.
48. Tunyasuvunakool K, Adler J, Wu Z, Green T, Zielinski M, Žídek A, Bridgland A, Cowie A, Meyer C, Laydon A, et al. Highly accurate protein structure prediction for the human proteome. Nature. 2021;596(7873):590–596.

49. Del Prete S, Isik S, Vullo D, De Luca V, Carginale V, Scozzafava A, Supuran CT, Capasso C. DNA cloning, characterization, and inhibition studies of an α-carbonic anhydrase from the pathogenic bacterium *Vibrio cholerae*. J Med Chem. 2012;55(23):10742–10748.
50. Schrödinger Release 2021-4. Maestro, Glide, Protein Preparation Wizard, Epik, SiteMap, QikProp, MacroModel, Desmond, Prime. New York (NY): Schrödinger, LLC; 2021.
51. Filipski KJ, Varma MV, El-Kattan AF, Ambler CM, Ruggeri RB, Goosen TC, Cameron KO. Intestinal targeting of drugs: rational design approaches and challenges. Curr Top Med Chem. 2013;13(7):776–802.
52. Anthouard R, DiRita VJ. Small-molecule inhibitors of toxT expression in *Vibrio cholerae*. mBio. 2013;4(4):e00403–e00413.
53. Vullo D, Del Prete S, De Luca V, Carginale V, Ferraroni M, Dedeoglu N, Osman SM, AlOthman Z, Capasso C, Supuran CT. Anion inhibition studies of the β-carbonic anhydrase from the pathogenic bacterium *Vibrio cholerae*. Bioorg Med Chem Lett. 2016;26(5):1406–1410.
54. Del Prete S, Vullo D, De Luca V, Carginale V, Ferraroni M, Osman SM, AlOthman Z, Supuran CT, Capasso C. Sulfonamide inhibition studies of the β-carbonic anhydrase from the pathogenic bacterium *Vibrio cholerae*. Bioorg Med Chem. 2016;24(5):1115–1120.
55. Greenwood JR, Calkins D, Sullivan AP, Shelley JC. Towards the comprehensive, rapid, and accurate prediction of the favorable tautomeric states of drug-like molecules in aqueous solution. J Comput Aided Mol Des. 2010;24(6-7):591–604.
56. Shelley JC, Cholleti A, Frye LL, Greenwood JR, Timlin MR, Uchimaya M. Epik: a software program for pK (a) prediction and protonation state generation for drug-like molecules. J Comput Aided Mol Des. 2007;21(12):681–691.
57. Bozdag M, Ferraroni M, Ward C, Carta F, Bua S, Angeli A, Langdon SP, Kunkler IH, Al-Tamimi AS, Supuran CT. Carbonic anhydrase inhibitors based on sorafenib scaffold: Design, synthesis, crystallographic investigation and effects on primary breast cancer cells. Eur J Med Chem. 2019;182:111600.
58. Behnke CA, Le Trong I, Godden JW, Merritt EA, Teller DC, Bajorath J, Stenkamp RE. Atomic resolution studies of carbonic anhydrase II. Acta Crystallogr D Biol Crystallogr. 2010; 66(Pt 5):616–627.
59. Ferraroni M, Del Prete S, Vullo D, Capasso C, Supuran CT. Crystal structure and kinetic studies of a tetrameric type II β-carbonic anhydrase from the pathogenic bacterium *Vibrio cholerae*. Acta Crystallogr D Biol Crystallogr. 2015;71(Pt 12): 2449–2456.
60. Farid R, Day T, Friesner RA, Pearlstein RA. New insights about HERG blockade obtained from protein modeling, potential energy mapping, and docking studies. Bioorg Med Chem. 2006;14(9):3160–3173.
61. Sherman W, Day T, Jacobson MP, Friesner RA, Farid R. Novel procedure for modeling ligand/receptor induced fit effects. J Med Chem. 2006;49(2):534–553.
62. Sherman W, Beard HS, Farid R. Use of an induced fit receptor structure in virtual screening. Chem Biol Drug Des. 2006; 67(1):83–84.
63. Friesner RA, Murphy RB, Repasky MP, Frye LL, Greenwood JR, Halgren TA, Sanschagrin PC, Mainz DT. Extra precision glide: docking and scoring incorporating a model of hydrophobic enclosure for protein-ligand complexes. J Med Chem. 2006;49(21):6177–6196.
64. Halgren TA, Murphy RB, Friesner RA, Beard HS, Frye LL, Pollard WT, Banks JL. Glide: a new approach for rapid, accurate docking and scoring. 2. Enrichment factors in database screening. J Med Chem. 2004;47(7):1750–1759.
65. Friesner RA, Banks JL, Murphy RB, Halgren TA, Klicic JJ, Mainz DT, Repasky MP, Knoll EH, Shelley M, Perry JK, et al. Glide: a new approach for rapid, accurate docking and scoring. 1. Method and assessment of docking accuracy. J Med Chem. 2004;47(7):1739–1749.
66. Jacobson MP, Pincus DL, Rapp CS, Day TJ, Honig B, Shaw DE, Friesner RA. A hierarchical approach to all-atom protein loop prediction. Proteins. 2004;55(2):351–367.
67. Jacobson MP, Friesner RA, Xiang Z, Honig B. On the role of the crystal environment in determining protein side-chain conformations. J Mol Biol. 2002;320(3):597–608.
68. Kim S, Yeon J, Sung J, Jin MS. Crystal structure of β-carbonic anhydrase CafA from the fungal pathogen *Aspergillus fumigatus*. Mol Cells. 2020;43(9):831–840.
69. UniProt Consortium. UniProt: the universal protein knowledgebase in 2023. Nucleic Acids Res. 2023;51(D1):D523–D531.
70. Camacho C, Coulouris G, Avagyan V, Ma N, Papadopoulos J, Bealer K, Madden TL. BLAST+: architecture and applications. BMC Bioinformatics. 2009;10:421.
71. Somalinga V, Buhrman G, Arun A, Rose RB, Grunden AM. A high-resolution crystal structure of a psychrohalophilic α-carbonic anhydrase from *Photobacterium profundum* reveals a unique dimer interface. PLOS One. 2016;11(12):e0168022.
72. Park HM, Park JH, Choi JW, Lee J, Kim BY, Jung CH, Kim JS. Structures of the γ-class carbonic anhydrase homologue YrdA suggest a possible allosteric switch. Acta Crystallogr D Biol Crystallogr. 2012;68(Pt 8):920–926.
73. Bowers KJ. Scalable algorithms for molecular dynamics simulations on commodity clusters. SC '06: Proceedings of the 2006 ACM/IEEE Conference on Supercomputing; Tampa, FL, USA; 2006, p. 43.
74. PyMOL. The PyMOL Molecular Graphics System, Version 2.5 Schrödinger, LLC, 2021.
75. Mugnaini C, Sannio F, Brizzi A, Del Prete R, Simone T, Ferraro T, De Luca F, Corelli F, Docquier JD. Screen of unfocused libraries identified compounds with direct or synergistic antibacterial activity. ACS Med Chem Lett. 2020; 11(5):899–905.
76. Clinical and Laboratory Standards Institute (CLSI). 2015. M07-A10: Methods for dilution antimicrobial susceptibility tests for bacteria that grow aerobically; approved standard. 10th ed. Wayne (PA): Clinical and Laboratory Standards Institute.